https://doi.org/10.5194/egusphere-2026-2430
Preprint. Discussion started: 11 June 2026

Investigating aerosol-cloud interactions by fusing DOE ARM observations with ship tracks: A methodology

Haipeng Zhang[1], Tianle Yuan[1,2], Hua Song[2,3], J. Christine Chiu[4], and Jukka-Pekka Jalkanen[5]

[1]GESTAR-II, University of Maryland, Baltimore County, MD, USA
[2]Sciences and Exploration Directorate, Goddard Space Flight Center, Greenbelt, MD, USA
[3]Science Systems and Applications, Inc., Lanham, MD, USA
[4]Department of Atmospheric Science, Colorado State University, Fort Collins, CO, USA
[5]Finnish Meteorological Institute, Helsinki, Finland

Correspondence to: Tianle Yuan (tianle.yuan@nasa.gov)

Abstract. Aerosol-cloud interactions (ACIs) remain one of the largest uncertainties in Earth's climate system, partly because large-scale meteorology can independently influence both aerosols and clouds, complicating causal attribution. To leverage the rich ground-based measurements from Atmospheric Radiation Measurement (ARM) campaigns and improve aerosol effect attribution, we develop an approach to identify ship-emission-influenced observation cases through source tracing. The method detects local peaks in cloud condensation nuclei number concentrations (N_{CCN}) and applies 24 h backward trajectories to determine whether the sampled air masses intersect ship emissions in the past day. Applying this framework to the ARM Eastern North Atlantic (ENA) observations in 2023 yields several dozen ship influenced cases, including a stratocumulus case in which two ship plumes contribute to a pronounced N_{CCN} enhancement. An increase in cloud fraction and liquid water path, along with a 1 h delay in precipitation, is observed by the comprehensive ARM measurements at the time of the N_{CCN} spike. As large-scale meteorological conditions remain steady, the cloud responses are more likely an aerosol-driven signal rather than meteorology-mediated covariability. Preliminary application to the Marine ARM GPCI Investigation of Clouds (MAGIC) campaign is also discussed. This framework provides a basis for building a multi-year, multi-site library of ship-emission-influenced cloud measurements, offering improved observational constraints for ACI research and model evaluation.

1 Introduction

Marine boundary layer clouds play a crucial role in regulating Earth's climate due to their extensive coverage and strong ability to reflect incoming solar radiation (Hahn and Warren, 2007; Warren et al., 1988). A 4% increase in stratocumulus coverage can offset the warming induced by doubling carbon dioxide concentrations (Randall et al., 1984). These clouds are highly sensitive to atmospheric aerosols, which act as cloud condensation nuclei (CCN) and can modify their micro/macro-physical properties. Increases in aerosol number concentrations can enhance cloud droplet number and reduce droplet size, effectively brightening the clouds (Twomey, 1977). Aerosols can also alter cloud fraction and liquid water path (LWP) through a range

https://doi.org/10.5194/egusphere-2026-2430
Preprint. Discussion started: 11 June 2026

of processes like precipitation suppression and entrainment drying (Ackerman et al., 2004; Albrecht, 1989; Qiu et al., 2024; Wang et al., 2011), known as cloud adjustments, thereby influencing cloud radiative effects (CREs). Despite their climatic importance, aerosol-cloud interactions (ACIs) remain one of the largest uncertainties in physical process understanding and long-term projections (Bellouin et al., 2020).

A key challenge in understanding ACIs is disentangling causal aerosol effects from observed relationships between aerosols and cloud properties, which are often shaped by covariability imposed by large-scale meteorology. For example, George and Wood (2010) found a negative temporal relationship between cloud droplet number concentrations (N_d) and LWP because a strengthening subtropical high reduced boundary-layer depth and LWP while increasing offshore aerosol transport. Similar meteorology-driven covariability also appears spatially (Goren et al., 2025; Mülmenstädt et al., 2024), such as over oceans near the west coasts of the continents where larger LWP occurs farther offshore while aerosol concentrations decrease with distance from continental sources. In this regard, opportunistic experiments such as ship tracks provide a powerful means to overcome these limitations (Christensen et al., 2022). The localized and well-defined aerosol perturbations generated by ships produce clear contrasts with the surrounding background cloud field, allowing more confident isolation of aerosol impacts on cloud properties and CREs. Therefore, ship-track studies provide a more causal view of cloud physical and radiative responses to aerosols than bulk statistical correlations alone.

Recent studies show that ship-emitted aerosols increase N_d and reduce cloud droplet size, thereby brightening marine clouds (Benas et al., 2025; Christensen et al., 2022; Diamond et al., 2020; Toll et al., 2019; Yuan et al., 2023, 2024). Beyond these microphysical effects, ship tracks have also been associated with changes in cloud fraction and LWP. Increases in cloud fraction have been found under clean background conditions (Yuan et al., 2023), whereas more subtle and limited cloud fraction changes are reported by Benas et al. (2025). LWP responses span both positive and negative changes, subject to environment conditions (Chen et al., 2012; Christensen and Stephens, 2011; Hu et al., 2021; Yuan et al., 2023). In terms of timing, microphysical changes appear within hours of emission, whereas cloud fraction and LWP adjustments evolve more slowly and depend strongly on meteorology (Gryspeerdt et al., 2021). It is also worth noting that the radiative forcing due to detectable ship tracks commonly considered in previous studies accounts for only a small fraction (~5%) of the total forcing from ship emissions, with the majority arising from non-detectable/virtual ship tracks (Yuan et al., 2025b). Ship-track studies have focused on satellite data, imposing limitations on understanding ACIs. For example, satellite-retrieved N_d is not independent of LWP as both are primarily derived from cloud effective radius and cloud optical depth. Satellite retrievals also provide little vertical information on boundary-layer structures and are subject to uncertainties in retrieved cloud properties and precipitation.

Ground-based observations, such as those from the U.S. Department of Energy's (DOE) Atmospheric Radiation Measurement (ARM) program, provide rich measurements of aerosol and clouds (particularly independent measurements of N_d, LWP, and cloud fraction, as well as their temporal evolution) and boundary-layer structures. These observations offer a pathway to address the limitations of satellite-based ship-track studies: Ship emissions enable ARM observations to be explicitly tagged

https://doi.org/10.5194/egusphere-2026-2430
Preprint. Discussion started: 11 June 2026

with a well-defined aerosol source, while comprehensive ARM measurements allow detailed examination of how this specific aerosol source influences cloud properties. Mace et al. (2026) performed a composite analysis of cloud responses to reduced shipping emissions before and after 2020 using ARM observations at the Eastern North Atlantic site (ENA; Wang et al., 2019). However, process-level understanding remains limited due to the statistical nature of their analysis.

To fill the above gaps, we incorporate ship emission locations with the reanalysis wind fields via backward-trajectory analysis to determine when ship plumes influence the ARM sites at hourly timescales. Cloud responses are then assessed by comparing ARM measurements during ship-influenced periods with those during clean background periods. To demonstrate this framework, we present two case studies that integrate ARM observations with ship emission data: one from ENA and another from the Marine ARM GPCI Investigation of Clouds campaign (MAGIC; Lewis, 2016). ENA provides long-term observations at a fixed site on Graciosa Island in the Azores while MAGIC was a short-term shipborne deployment along the Los Angeles-Honolulu route focused on the stratocumulus-to-cumulus transition. These examples lay the foundation for future long-term and statistical assessments of ship-emission-induced cloud responses through ground-based observations. The paper is organized as follows. Section 2 describes the datasets and the methodology for combining ARM observations with ship emission information for ACI analysis. Section 3 presents two illustrative cases of ship emission impacts on cloud properties. Section 4 provides the conclusion and discussion.

2 Data and Methodology

2.1 ARM observations and ERA5 reanalysis

Our first case utilizes a comprehensive suite of observations from the ARM ENA site on Graciosa Island (39.0911° N, 28.0267° W), which is characterized by marine stratocumulus clouds, to understand ACIs and boundary-layer processes. We adopt variables of year-long measurements (2023), including CCN number concentrations (N_{CCN}), cloud properties, precipitation, surface turbulent fluxes, boundary-layer structure, and Doppler-radar-derived dynamical quantities.

LWP is retrieved from the three-channel microwave radiometer that measures liquid water along the line-of-sight path through a statistical retrieval algorithm (Cadeddu et al., 2013; Turner et al., 2007). Cloud fraction is derived from the radar and lidar measurements in ARM Active Remote Sensing of CLouds (ARSCL) data (Clothiaux et al., 2000), available in the ARM Best Estimate Data Product (Xie et al., 2010). The low-cloud fraction is determined by the maximum cloud fraction below 3 km. Since the ARSCL cloud fraction is based on temporal frequency, we also use VISST-retrieved cloud fractions from Geostationary Operational Environmental Satellite (GOES) observations to provide horizontal coverage information (Minnis et al., 2008). Cloud base height is measured by the ceilometer (Morris, 2016). Surface downwelling shortwave and longwave radiations are obtained from the Surface Energy Balance System (SEBS). N_{CCN} is measured by a Dual Column CCN Counter operating in a supersaturation ramping mode (Uin and Enekwizu, 2024). We use N_{CCN} measured at 0.4% supersaturation for our analysis due to frequent stratus cloud supersaturation being above 0.3% reported by Hudson et al. (2010). The surface

https://doi.org/10.5194/egusphere-2026-2430
Preprint. Discussion started: 11 June 2026

95 precipitation rate is measured by optical rain gauge (ORG) and present weather detector (PWD) from the Surface Meteorological System (MET) (Kyrouac and Tuftedal, 2024). Because the PWD-measured precipitation rate agrees more closely with radar reflectivity (introduced later) in both phase and magnitude than the ORG (Figure 6 vs. Figure A1), we adopt the PWD measurement in our analysis. Surface turbulent fluxes, including latent heat flux and sensible heat flux, are measured by the ECOR eddy-covariance system (Cook and Sullivan, 2020).

100 To characterize vertical structure of cloud and precipitation, we also use radar reflectivity obtained from the Ka-band ARM Zenith Radar (KAZR) (Widener et al., 2012). Vertical velocity and its higher-order moment (variance) are obtained from Doppler Lidar Vertical Velocity Statistics Value-Added Product (VAP) (Newsom et al., 2025). The planetary boundary layer height (PBLH) is retrieved from radiosondes using the Heffter method (Heffter, 1980). All variables and associated products used are summarized in Table 1, and are resampled to hourly resolution to maintain consistency across instruments unless 105 specified otherwise.

Our second case is based on the MAGIC field campaign, which deployed the ARM Mobile Facility aboard a commercial cargo ship traveling between Los Angeles and Honolulu for a full year (2012-2013). It collected continuous observations of clouds, aerosols, precipitation, radiation, and atmospheric structure across the stratocumulus-to-cumulus transition zone (Lewis, 2016). In this case, N_{CCN} is used only.

110 In addition to ARM observations, we also obtain large-scale meteorological fields from the ERA5 reanalysis (Hersbach et al., 2020). They are used to derive horizontal temperature and moisture advection, the estimated inversion strength (EIS), and large-scale vertical velocity at 700 hPa. The ERA5 data are interpolated to the site location to match instrument measurements.

Table 1. Ground-based measurements, satellite data, and ERA5 reanalysis used in this study.

Variables	Resolution Time / Vertical	Instrument	Products and Reference
Liquid water path	1-3 s / -	Microwave Radiometer, 3 Channel (MWR3C)	enamwr3cC1.b1 (Turner et al., 2007) (Cadeddu et al., 2013)
Cloud fraction	1 h / 30 m	Derived from the radar and lidar measurements in ARSCL data	enaarmbecldradC1.c1 (Clothiaux et al., 2000) (Xie et al., 2010)
Cloud base height	16 s / -	Ceilometer	enaceilC1.b1 (Morris, 2016)
N_{CCN}	75 min / -	Dual Column CCN Counter	enaaosccn2colaspectraC1.b1* (Uin and Enekwizu, 2024)
Surface precipitation rate	1 min / -	Optical Rain Gauge and Present Weather Detector	enametC1.b1 (Kyrouac and Tuftedal, 2024)
Latent heat flux and sensible heat flux	30 min / -	ECOR eddy-covariance system	ena30qcecorC1.c1

https://doi.org/10.5194/egusphere-2026-2430
Preprint. Discussion started: 11 June 2026

			(Cook and Sullivan, 2020)
Radar reflectivity	2 s / 30 m	Ka-Band ARM Zenith RADAR 2nd generation (KAZR2)	enakazr2cfrcorgeC1.c0 (Widener et al., 2012)
Vertical velocity and its variance	10 min / 30 m	Doppler Lidar	enadlprofwstats4newsC1.c1 (Newsom et al., 2025)
PBLH	Twice a day / -	Radiosonde	enapblhtsonde1mcfarlC1.c1 (Heffter, 1980)
Surface downwelling shortwave and longwave hemispheric irradiance	1 min / -	Surface Energy Balance System	enaqcrad1longC1.c2 (Long and Shi, 2006)
Cloud fraction	1 h / -	GOES	enaarmbecldradC1.c1 (Minnis et al., 2008)
Horizontal temperature and moisture advection, EIS, and large-scale vertical velocity at 700 hPa	1 h / -	-	ERA5 reanalysis (Hersbach et al., 2020)

*This product is used for ENA. For MAGIC, the "magaosccn100M1.a1" dataset is adopted with a 1 s temporal resolution.

2.2 Ship emissions and virtual ship tracks

Ship emissions and ship tracks provide the pollution source information for ENA and MAGIC, respectively. The ship emission dataset consists of the location of hourly SOx emission on a 0.01° spatial grid for the year 2023, which covers the area around ENA.

For MAGIC, as the ship emission data are unavailable during the campaign period, the virtual ship-track dataset near California from Yuan et al. (2025a) is used instead to provide ship pollution sources. Virtual ship tracks are simulated tracks that identify likely ship-polluted clouds when visible ship tracks are absent in satellite imagery. To construct them, ship locations are first obtained from the Automatic Identification System (AIS). For each Moderate Resolution Imaging Spectroradiometer (MODIS) overpass, AIS records from the preceding 30 hours are used so that the resulting virtual ship tracks match what MODIS would observe at that time. Air parcels are then released at these ship locations and advected forward using the NOAA HYSPLIT model (Rolph et al., 2017; Stein et al., 2015) through MERRA2 reanalysis data (Gelaro et al., 2017), with each trajectory terminated at the MODIS overpass time. The AIS-reported starting location and the HYSPLIT-projected ending location from virtual ship tracks are used as pollution sources for the MAGIC case analysis.

2.3 Approach to identify cloud measurements that are affected by ship emissions

We identify ship-emission-affected cloud measurements (hourly) at ENA and MAGIC by assuming that ship-emitted aerosols reaching the site produce detectable CCN enhancements whose origin can be traced back to specific ship locations. This leads to a two-step procedure: CCN peaks are first used to flag candidate cases, since sharp CCN peaks above the background more

https://doi.org/10.5194/egusphere-2026-2430
Preprint. Discussion started: 11 June 2026

likely signal the arrival of ship emissions. Backward trajectory analysis is then used to verify the link to ship emission sources. Specifically, in the first step, the time series of hourly N_{CCN} at 0.4% supersaturation are examined for pronounced local peaks, defined as instances where the CCN concentration exceeds both the 5 h mean before and after the event by at least a factor of 1.5 and also exceeds an absolute threshold of 100 cm^{-3}. This initial screening helps isolate pulses of local CCN peaks, possibly related to ship-related perturbations. We further refine our preliminary set by selecting only the cloudy cases. Second, for each identified peak, a 24 h backward trajectory is computed using the HYSPLIT model driven by 1° Global Data Assimilation System (GDAS) wind fields. Assuming that ship emissions are transported within the lower boundary layer, the trajectory is initialized at the 300-m height level on an isobaric surface, consistent with Ghate et al. (2023). A case is identified as influenced by ship emissions if any position along the backward trajectory is within a distance threshold (10 km) of a ship at the corresponding time. In this regard, an identified case might be co-influenced by multiple ships.

Figure 1 demonstrates how the initial height used in the trajectory calculations and the distance threshold influence the number of identified ship-emission-affected cases at ENA. The sensitivity to initial height is modest. The trajectories initialized at 100 m, 200 m, and 300 m yield nearly identical results, with only minor differences at thresholds below 5 km where trajectory paths are most sensitive to initial vertical placement. By contrast, increasing the distance threshold leads to a rapid rise in detected cases, which saturates at roughly 10 km. This number coincidentally corresponds to the average ship-track width that is approximately 10 MODIS pixels (Yuan et al., 2025a). Kivekäs et al. (2014) also reported that ship plumes about 50 km downwind of a major shipping lane (plume age ~1 h) are still measurable. Therefore, selecting a 10 km threshold allows to retain more case samples while still capturing detectable ship emission influences at the ENA site.

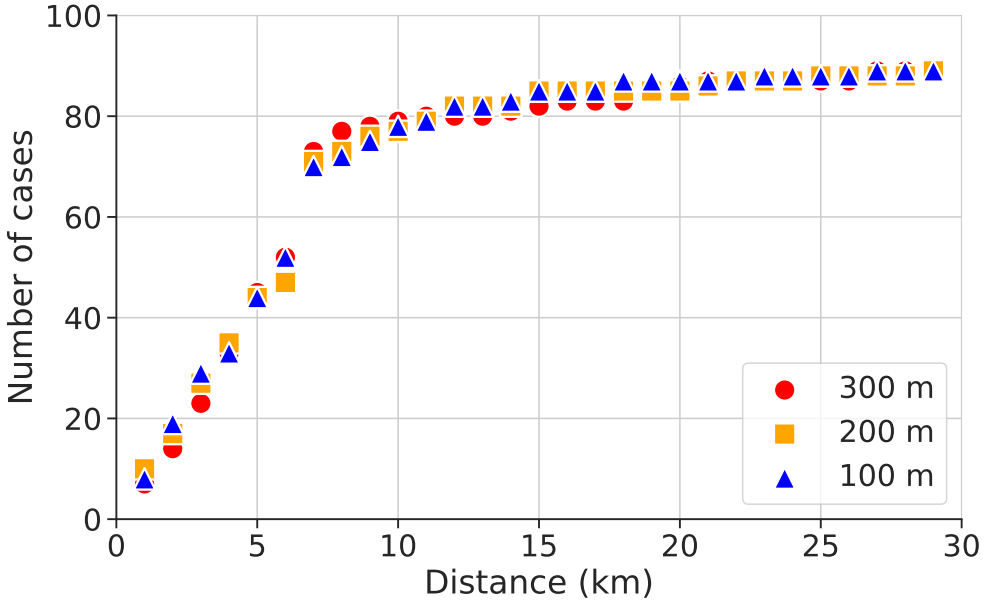

https://doi.org/10.5194/egusphere-2026-2430
Preprint. Discussion started: 11 June 2026

Figure 1: Number of ship-emission-affected cases as a function of the distance threshold between the air mass along the backward trajectory and a ship emission location for the ENA case. Results for different initial height levels are shown in distinct colors.

3 Results

The above approach is applied to both the ENA and MAGIC observations. Because the ship emission dataset provides far more emission locations than those available from virtual ship tracks, the method yields more identified cases at ENA and one potential case from MAGIC. Consequently, our analysis focuses primarily on a representative ENA case in terms of how it is identified and how clouds respond to ship emissions, while also briefly discussing the limitations of case identification in the MAGIC dataset.

3.1. An illustrative stratocumulus case at ENA

Following the first step of our approach, we identified approximately 2250 candidate cloudy cases from the ENA observations in 2023. Among these, 79 cases are found to be influenced by ship emissions after applying the backward trajectory screening (the second step of our approach). Examination of radar reflectivity shows that these cases span a range of cloud types, including stratocumulus, shallow cumulus, and deep convection. In this study, we focus on a stratocumulus case observed at 1800 UTC on December 21, 2023 (Local Solar Time = UTC − 2 h), for detailed analysis. Near 1800 UTC, the cloud field around the site is dominated by a relatively homogeneous low-cloud deck (Figure A2), with little mid- and high-level clouds (Figure A3). The N_{CCN} at 0.4% supersaturation for this case reaches approximately 420 cm^{-3}, which is substantially higher than the December monthly average of about 150 cm^{-3}.

Figure 2 presents a backward trajectory analysis for this stratocumulus case. The air mass here is traced back in time, with its location shown at the initial time (Figure 2a) and 4 h earlier (Figure 2b). At each of these times, the locations of nearby ship emissions (gray dashes) are also plotted. The case is likely affected by two ship emission plumes. The first one comes from a ship that passes close to the ENA site at the time of the event (Figure 2a). By tracing the air masses back in time, we further find that the ENA site is also influenced by a southeastward ship emission plume that was emitted about 4 h earlier, with a distance of 3 km to the trajectory. This southeastward transport is due to the presence of an anticyclone over the ENA region, as shown in Figure 3. The combined effect of these two plumes contributes to the local N_{CCN} peak observed at 1800 UTC. While the N_{CCN} spike is very likely driven by ship emissions, we further examine whether local sources could contribute to this enhancement. For example, aircraft landing and take-off nearby may increase N_{CCN} (Gallo et al., 2020; Ghate et al., 2023). However, comparison with other days in December 2023 at 1800 UTC shows that the observed N_{CCN} for our selected case exceeds the monthly mean plus one standard deviation (182 + 142 cm^{-3}), indicating an anomalously high enhancement for the site and suggesting that local sources are unlikely to dominate in this case. We acknowledge, however, that a quantitative

https://doi.org/10.5194/egusphere-2026-2430
Preprint. Discussion started: 11 June 2026

assessment of local aircraft contributions is challenging here due to the lack of flight time schedule data (Gallo et al., 2020; Ghate et al., 2023).

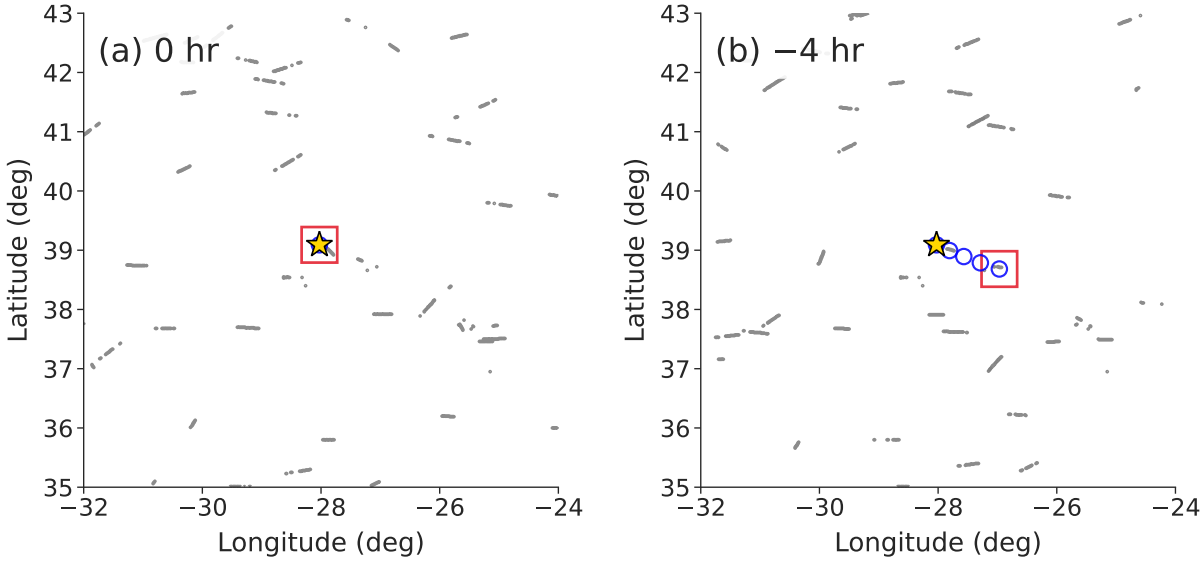

Figure 2: Backward air mass trajectory initiated at the ENA site at 18:00 UTC on 21 December 2023. (a) At the starting time, the air mass coincides with a ship emission location (indicated by gray dashes). (b) Four hours earlier, the air mass along the backward trajectory (blue circles) overlaps with a ship emission location. Overlap is defined as an air mass location within 10 km of an emission location, illustrated by the red box. The yellow star marks the ENA site.

https://doi.org/10.5194/egusphere-2026-2430
Preprint. Discussion started: 11 June 2026

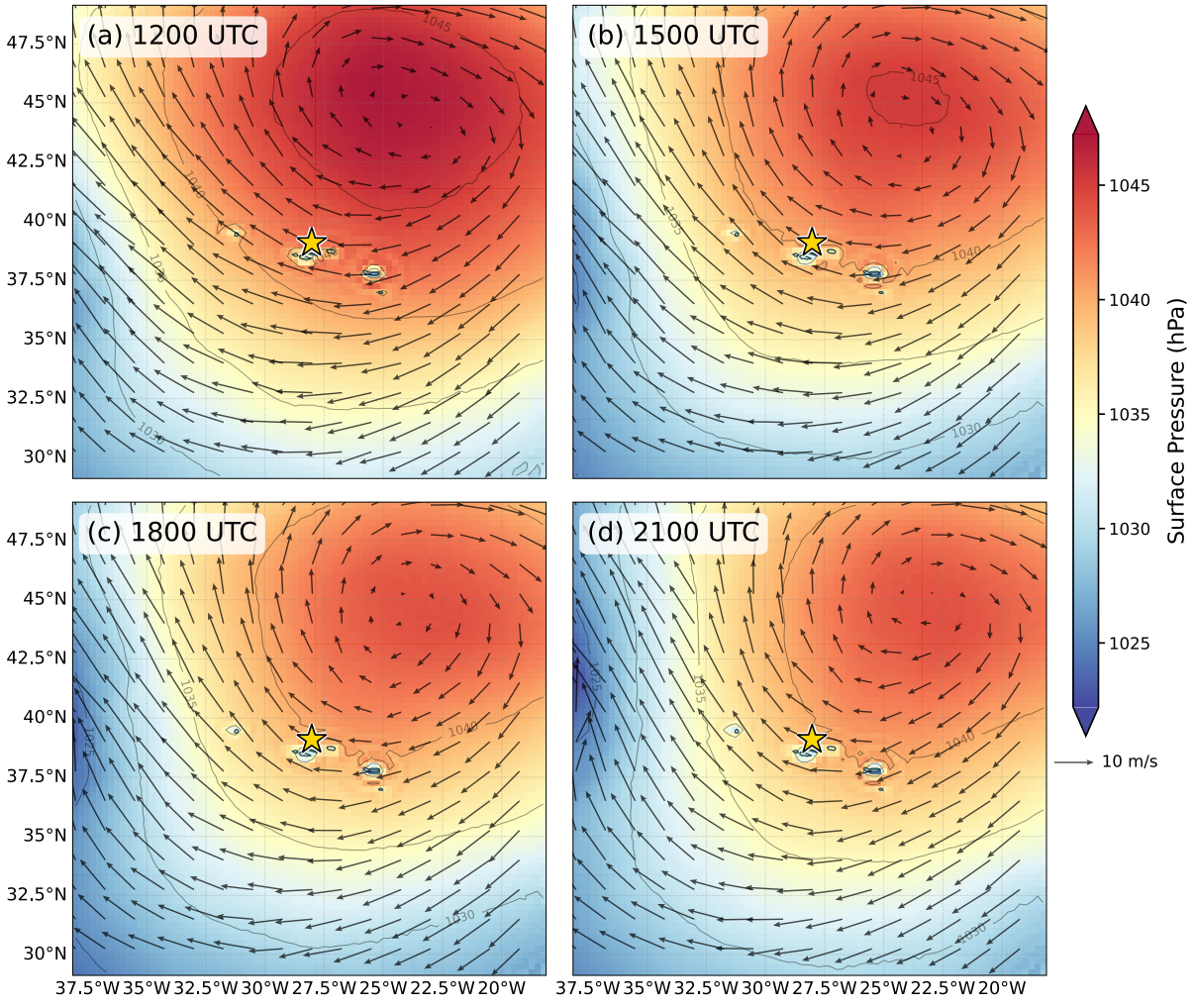

Figure 3: Maps of surface pressure at four times on December 21, 2023: (a) 1200 UTC, (b) 1500 UTC, (c) 1800 UTC, and (d) 2100 UTC. Arrows show the 10 m surface wind fields from ERA5, and the yellow star marks the ENA site.

195 The responses of cloud fraction and LWP to the aerosol perturbation are examined by comparing the clouds at the N_{CCN} peak time with those in the surrounding hours. This comparison is well suited because the ENA site remains under the influence of a surface high pressure system from 1200 UTC to 2100 UTC (Figure 3), which helps maintain relatively steady meteorological conditions, particularly near 1800 UTC, when the N_{CCN} peak occurs. Figure 4 presents the diurnal variation of hourly N_{CCN}, cloud properties, precipitation, and radiative fluxes on December 21, 2023. At the hour of the N_{CCN} peak, marked by the pink
200 bar, the LWP shows a distinct increase, while the low-cloud fraction reaches its maximum 1 h earlier and remains pronounced through the following hour. This behavior suggests that the ship emissions may enhance LWP and low-cloud fraction by

https://doi.org/10.5194/egusphere-2026-2430
Preprint. Discussion started: 11 June 2026

suppressing precipitation. The surface precipitation rate peaks 1 h later. This could suggest an aerosol-induced delay of the onset of precipitation, or due to fortuitous variability in cloud and precipitation. Although low-cloud fraction and LWP increase at the N_{CCN} peak, which would typically enhance shortwave reflection, downwelling shortwave radiative fluxes at the surface exhibit no noticeable drop, primarily because the event occurs in the late afternoon when solar radiation is already weak due to a high solar zenith angle. Downwelling longwave radiative fluxes, by contrast, show a clear increase at the N_{CCN} peak, consistent with increased cloud fraction and LWP.

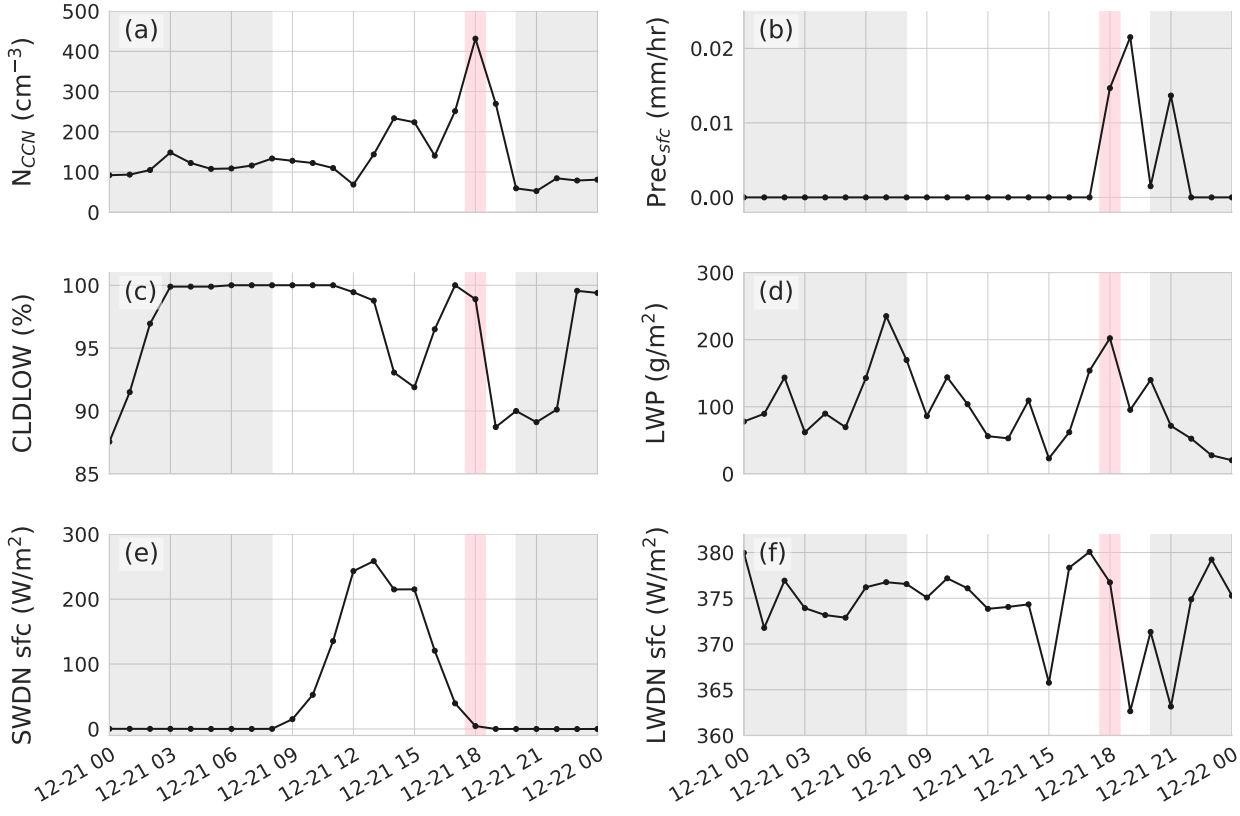

Figure 4: Time series (UTC) of hourly (a) N_{CCN} at 0.4% supersaturation, (b) surface precipitation rate, (c) low-cloud fraction from ARSCL, (d) liquid water path, (e) downward shortwave radiative fluxes at the surface, and (f) downward longwave radiative fluxes at the surface, observed at ENA on December 21, 2023. The gray shading marks the nighttime, and the pink bar indicates the time of the local N_{CCN} peak through the first-step screening procedure.

To investigate whether the cloud responses truly arise from the aerosol perturbation rather than meteorology-mediated covariability, we also examine the diurnal evolution of key meteorological variables, as shown in Figure 5. Overall, no

https://doi.org/10.5194/egusphere-2026-2430
Preprint. Discussion started: 11 June 2026

meteorological factor varies in phase with the changes in low-cloud fraction and LWP near the N_{CCN} spike, suggesting that the observed cloud responses are unlikely to be driven by meteorological variability. A closer examination shows that near the N_{CCN} peak, several meteorological variables remain relatively steady, including moisture advection (Figure 5b) and estimated inversion strength (Figure 5c), consistent with the stable synoptic conditions shown in Figure 3. Latent and sensible heat fluxes also show little variation around the N_{CCN} spike, which is expected because the event occurs in the late afternoon when solar radiation is already weak. We also notice an increase in cold-air temperature advection near the N_{CCN} peak (Figure 5a), which typically promotes an increase in low-cloud fraction by destabilizing the surface-atmosphere interface and enhancing upward buoyancy flux (Norris and Iacobellis, 2005), but this cannot account for the subsequent decline in low-cloud fraction after the N_{CCN} spike. Similarly, the enhancement of large-scale downdraft (Figure 5d) tends to dry clouds but does not align with the observed increase in low-cloud fraction and LWP at the N_{CCN} spike. Taken together, these factors indicate that large-scale meteorological influences are insufficient to explain the cloud changes observed in this case, and that the responses are more likely attributable to the aerosol perturbation.

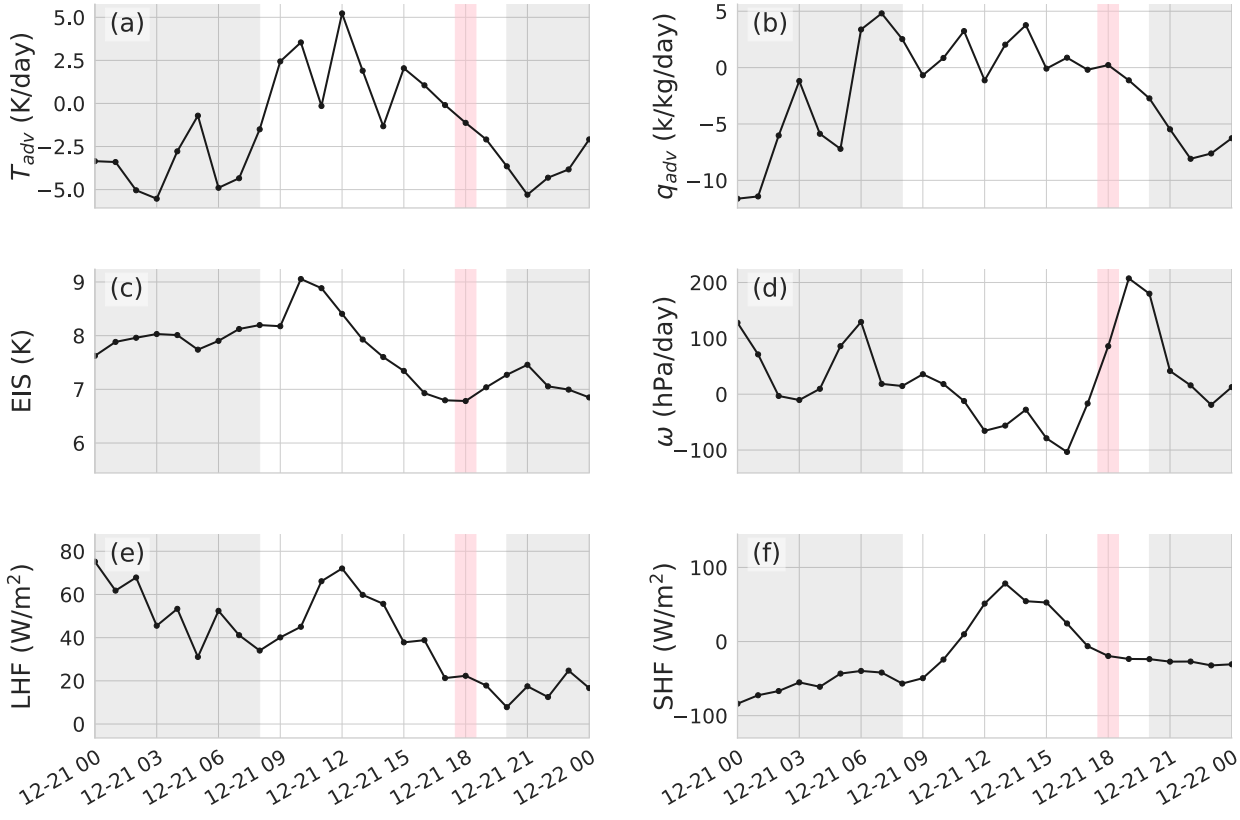

https://doi.org/10.5194/egusphere-2026-2430
Preprint. Discussion started: 11 June 2026

Figure 5: Same as Figure 4, but for hourly (a) horizontal temperature advection, (b) horizontal moisture advection, (c) estimated inversion strength, (d) large-scale vertical velocity at 700 hPa, (e) latent heat fluxes, and (f) sensible heat fluxes.

Figure 6 shows the high temporal resolution profile of cloud reflectivity and the precipitation rate, which provides a more detailed characterization of cloud responses to the aerosol perturbation. On the day of the selected case, the boundary layer is topped by stratocumulus and exhibits intermittent precipitation, much of which evaporates before reaching the surface. At the N_{CCN} peak time, marked by the pink bar, cloud reflectivity decreases relative to surrounding periods, indicating that precipitation is likely suppressed by the elevated aerosol loading. The precipitation appears to be delayed by approximately 1 h, as evidenced by stronger reflectivity and a pronounced surface precipitation rate immediately after the N_{CCN} peak. That said, the delayed precipitation may also be coincidental and not necessarily related to aerosol perturbations, and its significance should be evaluated with a larger sample of cases in the future. Figure 7 shows the vertical velocity and its variance, which offer insight into the role of local updrafts and boundary layer turbulence in shaping the cloud response. At the N_{CCN} peak, the upward vertical velocity (Figure 7a) is relatively weak compared with other times of the day, as is the boundary layer turbulence (Figure 7b). These conditions suggest that local updrafts and boundary layer turbulence make minor contributions to the observed changes in cloud properties. In contrast, the second precipitation peak is clearly associated with stronger updrafts, while the third peak is more consistent with enhanced boundary layer turbulence that can broaden cloud droplet size distribution and benefit drizzle formation (Borque et al., 2018). Note that the lidar-derived vertical velocities here may be biased low in drizzling boundary layers, where drizzle droplets contribute their fall speed to the retrieved signal (Newsom et al., 2025).

https://doi.org/10.5194/egusphere-2026-2430
Preprint. Discussion started: 11 June 2026

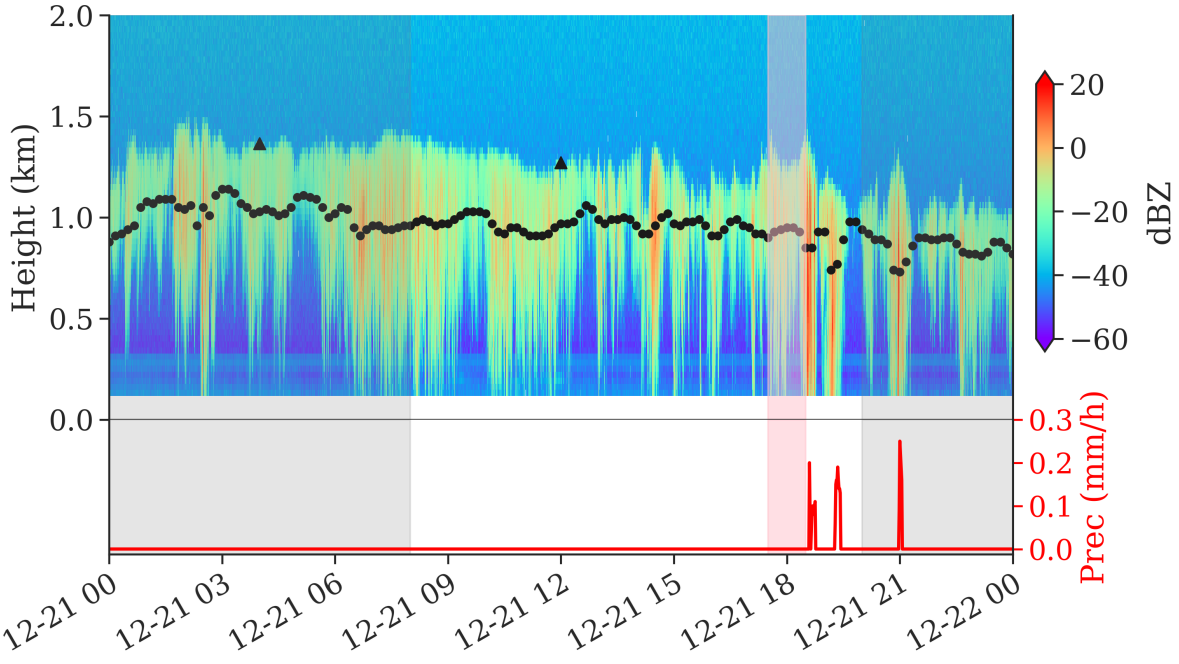

Figure 6: Height-time cross section of KAZR radar reflectivity (2 s resolution) on December 21, 2023 (UTC). The triangles mark the PBL height, and the dots indicate the cloud-base height. The red line shows the 1 min surface precipitation rate. The gray shading denotes nighttime, and the pink bar marks the time of the local N_{CCN} peak.

https://doi.org/10.5194/egusphere-2026-2430
Preprint. Discussion started: 11 June 2026

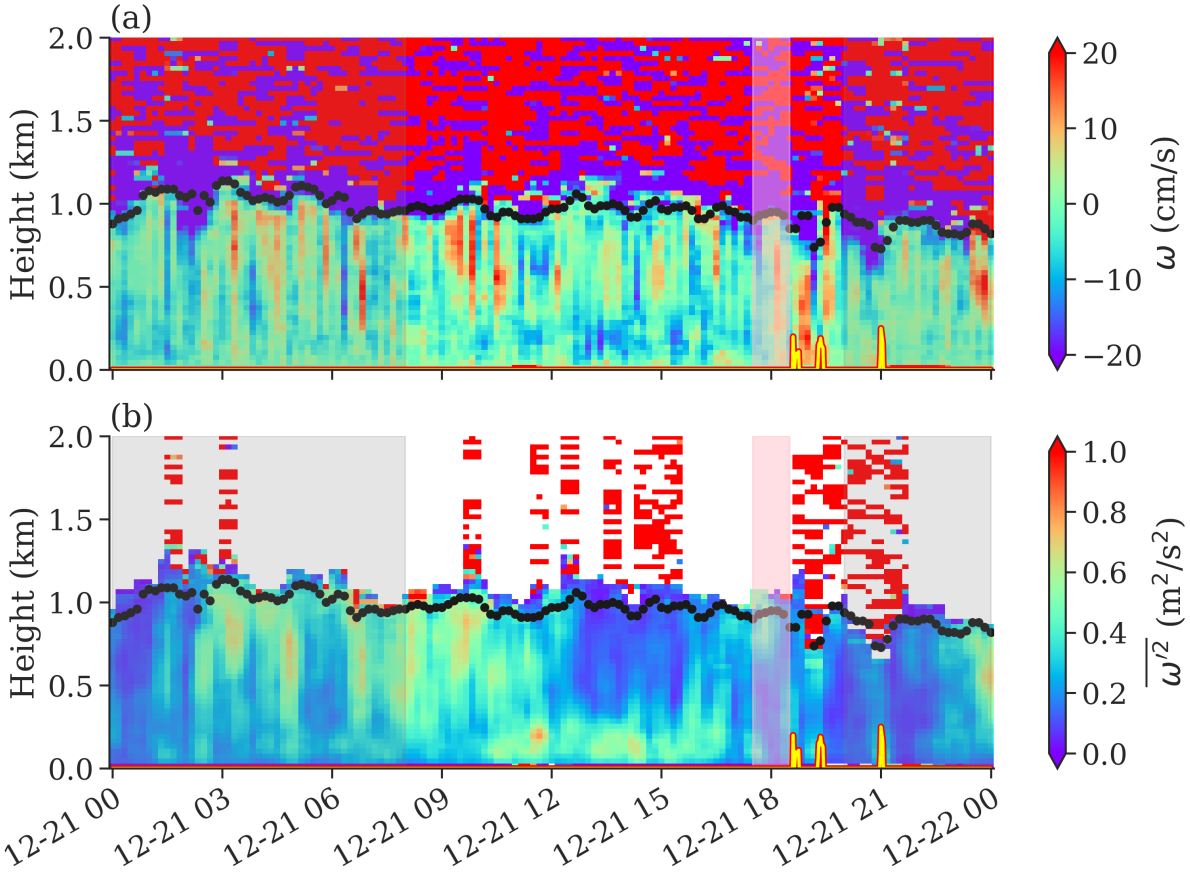

Figure 7: Similar to Figure 6, but for (a) vertical velocity and (b) its variance (10 min resolution). The dots mark the cloud-base height, and the red lines with yellow shading underneath show the surface precipitation rate.

260

3.2. A potential ship-emission-affected case during MAGIC

Compared to ENA, MAGIC has a much shorter observation period, potentially yielding fewer matched cases. Employing the first step of our approach to the MAGIC dataset, we identify approximately 130 candidate cases in total from 15 round-trip Lagrangian observations. For instance, in Leg05B, which represents the commercial vessel traveling from Hawaii to Los
265 Angeles from November 9 to 15 in 2012, four candidates with local aerosol spikes are found (Figure 8). However, after applying the second step of the method, we identify only one case in Leg05B that is most likely influenced by ship emissions. In this case, the closest distance between a position along the backward trajectory (the gray line) and the ship emission source (the blue square) is approximately 80 km (Figure 9). Although this distance is relatively large, it remains possible that the case is influenced by the ship plume. Such a limited number of cases occur primarily because the virtual ship-track data available

https://doi.org/10.5194/egusphere-2026-2430
Preprint. Discussion started: 11 June 2026

are temporally intermittent and spatially limited to regions near the California coast. We hope to obtain a more complete ship emission dataset to find more cases in the future.

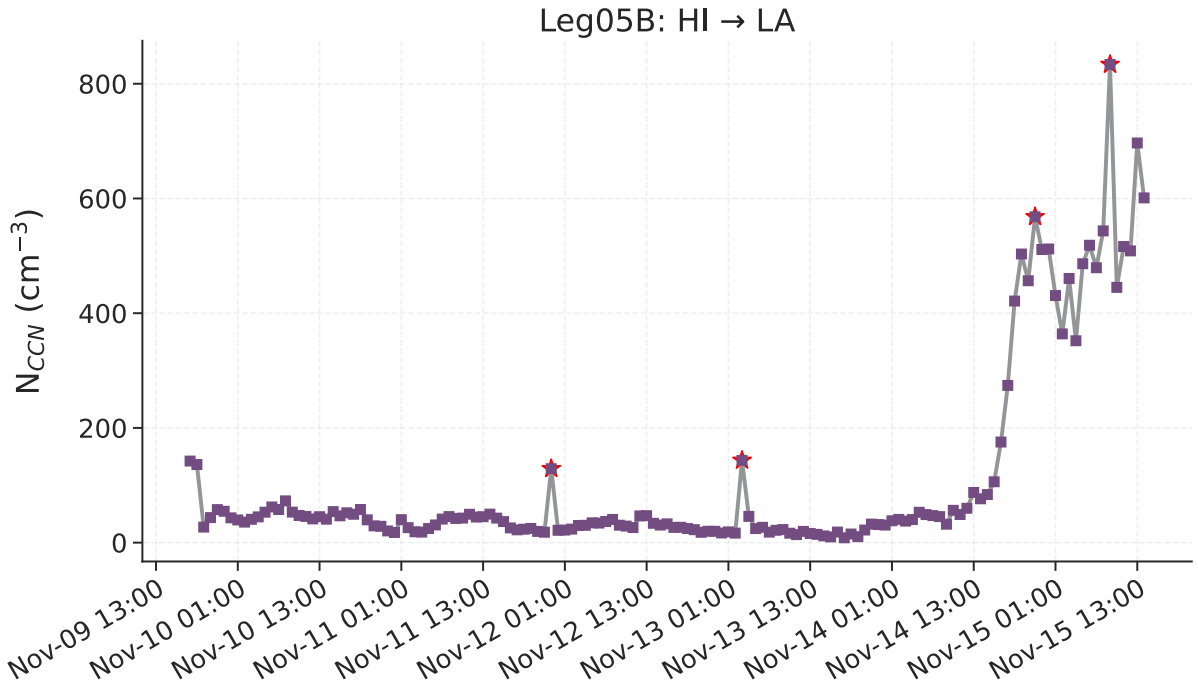

Figure 8: Time series of hourly N_{CCN} at 0.4% supersaturation observed during MAGIC Leg05B (Hawaii to California) from November 9 to 15, 2012 (UTC). The red star marks the time of the local N_{CCN} peak.

https://doi.org/10.5194/egusphere-2026-2430
Preprint. Discussion started: 11 June 2026

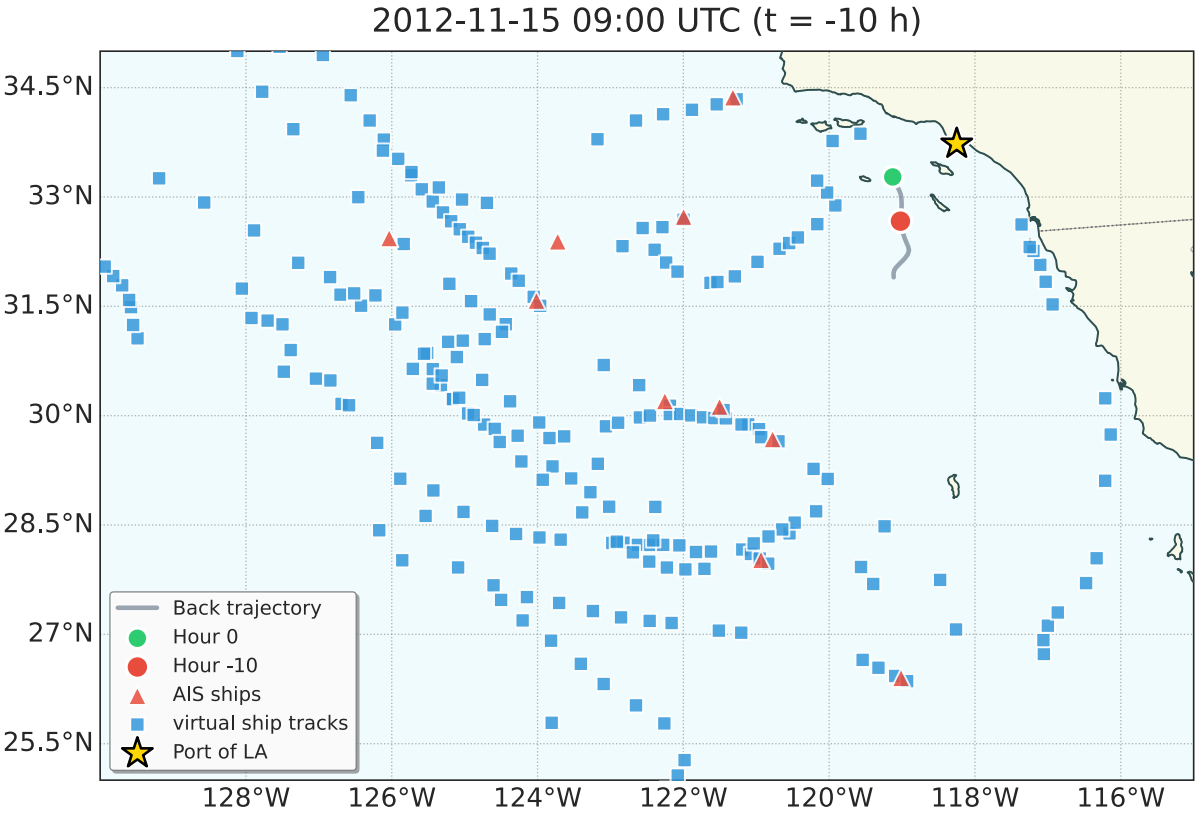

Figure 9: Gray line shows the 24 h backward trajectory starting at 0900 UTC on November 15, 2012 (green dot, hour 0) associated with the N_{CCN} peak case. The red dot indicates the trajectory location 10 h earlier (hour -10). Red triangles indicate vessel locations from AIS records, and blue squares mark the ending locations of the virtual ship tracks. The Port of Los Angeles is shown by the yellow star.

4. Conclusion and Discussion

In this study, we develop a method that integrates ship-track location information with ARM observations to more effectively identify and analyze aerosol influences on marine boundary layer clouds. Ship-emission-affected cases are identified by detecting local N_{CCN} spikes and then computing 24 h backward trajectories to determine whether the sampled air masses intersect ship emission locations a few hours earlier. Applying this method to both the ENA and MAGIC campaigns reveals several dozen ship-influenced cases at the ENA site in 2023, whereas only one potential case is found in the MAGIC dataset, largely due to the limited availability of ship-track information along the full routes. A stratocumulus case study at ENA further demonstrates increases in low-cloud fraction and LWP together with a 1 h delay in precipitation at the N_{CCN} peak time. These responses are found to be more likely attributed to aerosol perturbations than to meteorology-mediated covariability, as large-

https://doi.org/10.5194/egusphere-2026-2430
Preprint. Discussion started: 11 June 2026

scale meteorological conditions and turbulent mixing in the boundary layer do not vary in phase with the observed cloud changes.

These results highlight the value of leveraging ship emissions with ARM measurements and demonstrate the feasibility of building a multi-year, multi-site library of ship-emission-affected cases at ENA, MAGIC, and other coastal observatories (e.g., Eastern Pacific Cloud Aerosol Precipitation Experiment or EPCAPE (Russell et al., 2021)). Such a dataset would provide a unique foundation for ACI process studies using ARM measurements and observational constraints for model evaluation. In future work, we will also incorporate vertically resolved cloud and drizzle profiles of boundary-layer clouds retrieved from radar, lidar, and zenith radiance observations within a unified framework (Fielding et al., 2015), providing enhanced process-level insight into ACIs.

Several limitations, however, need to be considered. For example, a long record of ship emission data is required to compile the above libraries. Another challenge is separating ship-derived aerosol enhancements from those produced by local sources, such as airport activity, vehicles, or other island-based emissions. Such local signals can mimic ship plume N_{CCN} spikes and complicate attribution of the cloud responses. In addition, ship plumes undergo dilution as they are transported over long distances. Turbulent mixing and chemical processing weaken the aerosol signal with increasing plume age, making the influence of ship emissions less distinct and introducing greater uncertainty. This can be examined when concentrations of emission species become available. Overall, this combined framework offers a valuable pathway for enhancing causal understanding of ACIs and more accurate estimates of aerosol forcing.

https://doi.org/10.5194/egusphere-2026-2430
Preprint. Discussion started: 11 June 2026

Appendix A

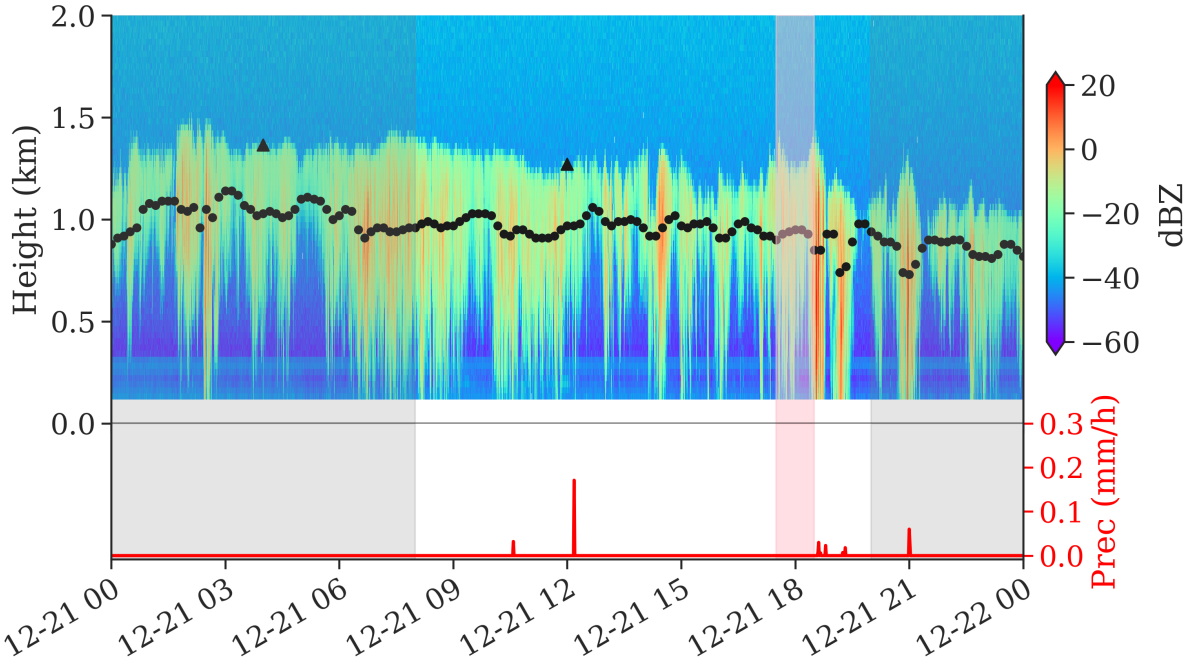

Figure A1: Same as Figure 6, but for the precipitation rate from ORG.

https://doi.org/10.5194/egusphere-2026-2430
Preprint. Discussion started: 11 June 2026

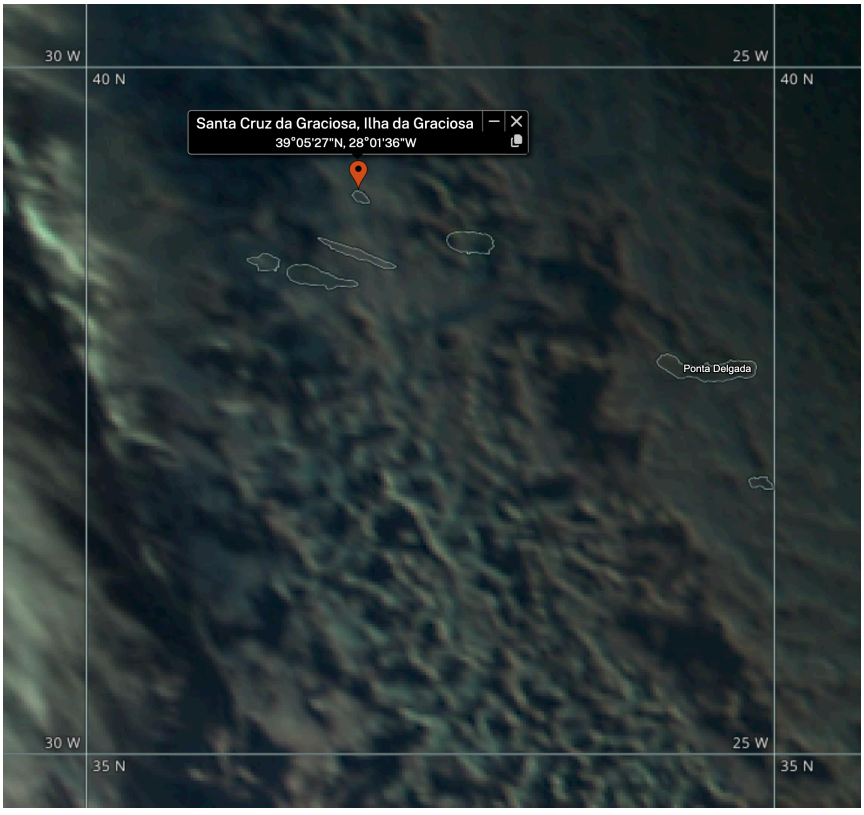

Figure A2: Natural Color RGB satellite imagery over Graciosa Island (red marker) on 21 December 2023 at 18:00 UTC, obtained from NASA Worldview (https://worldview.earthdata.nasa.gov). The composite is generated from 3-hourly geostationary satellite observations (Meteosat SEVIRI, GOES ABI, Himawari-9 AHI), with RGB channels assigned to NIR1.6, VIS0.8, and VIS0.6 reflectances. In this color scheme, water clouds appear white, ice clouds cyan, ocean black, and land brown.

https://doi.org/10.5194/egusphere-2026-2430
Preprint. Discussion started: 11 June 2026

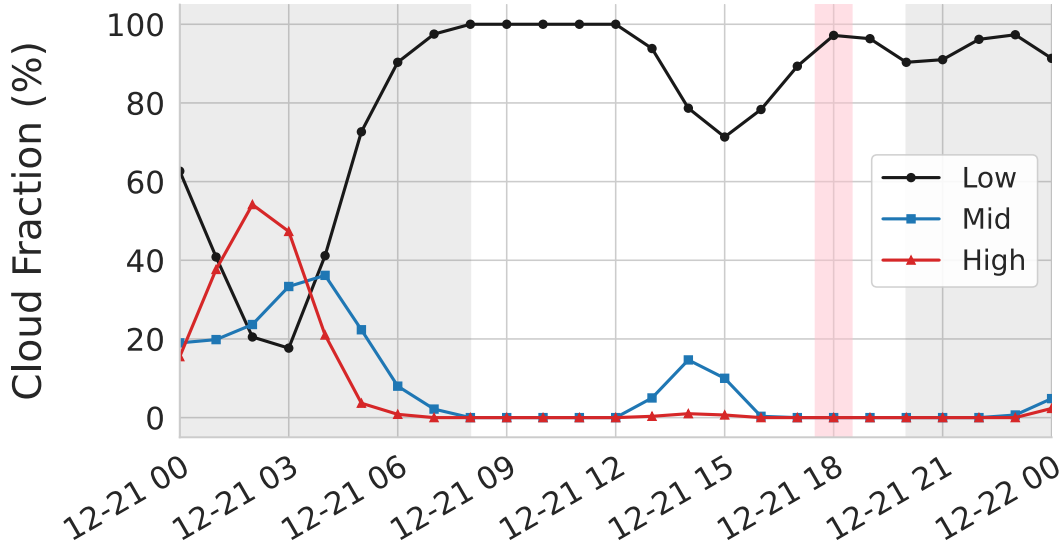

Figure A3: Same as Figure 4c, but for low-, mid-, and high-level cloud fraction from satellite measurements.

Data availability

The ENA and MAGIC observation data can be accessed at https://armgov.svcs.arm.gov/research/campaigns/aaf2017ace-ena and https://armgov.svcs.arm.gov/research/campaigns/amf2012magic, respectively. The ERA5 reanalysis data are available at https://cds.climate.copernicus.eu/datasets/reanalysis-era5-pressure-levels?tab=overview. The virtual ship-track data are available at https://dataverse.harvard.edu/dataset.xhtml?persistentId=doi:10.7910/DVN/X65MDV. The HYSPLIT tools are available at https://www.ready.noaa.gov/HYSPLIT.php.

Author contributions

TY and HZ contributed to the study conception and design. HZ, HS, and JJ collected data. HZ performed the simulations and analysis. HZ prepared the manuscript with contributions from all co-authors.

Competing interests

The authors declare no conflicts of interest relevant to this study.

https://doi.org/10.5194/egusphere-2026-2430
Preprint. Discussion started: 11 June 2026

Acknowledgements

This research used resources of the National Energy Research Scientific Computing Center (NERSC), a Department of Energy User Facility (project m4979). This study was supported by DOE ASR program (grant DE-SC0024078). Jukka-Pekka Jalkanen was supported by the Strategic Research Council at the Academy of Finland: Marine waterways as a sustainable source of wellbeing, security, and safety (Decision number: 365647).

References

Ackerman, A. S., Kirkpatrick, M. P., Stevens, D. E., and Toon, O. B.: The impact of humidity above stratiform clouds on indirect aerosol climate forcing, Nature, 432, 1014–1017, https://doi.org/10.1038/nature03174, 2004.

Albrecht, B. A.: Aerosols, Cloud Microphysics, and Fractional Cloudiness, Science (1979)., 245, 1227–1230, https://doi.org/10.1126/science.245.4923.1227, 1989.

Bellouin, N., Quaas, J., Gryspeerdt, E., Kinne, S., Stier, P., Watson-Parris, D., Boucher, O., Carslaw, K. S., Christensen, M., Daniau, A. L., Dufresne, J. L., Feingold, G., Fiedler, S., Forster, P., Gettelman, A., Haywood, J. M., Lohmann, U., Malavelle, F., Mauritsen, T., McCoy, D. T., Myhre, G., Mülmenstädt, J., Neubauer, D., Possner, A., Rugenstein, M., Sato, Y., Schulz, M., Schwartz, S. E., Sourdeval, O., Storelvmo, T., Toll, V., Winker, D., and Stevens, B.: Bounding Global Aerosol Radiative Forcing of Climate Change, Reviews of Geophysics, 58, 1–45, https://doi.org/10.1029/2019RG000660, 2020.

Benas, N., Meirink, J. F., Roebeling, R., and Stengel, M.: Analysis of ship emission effects on clouds over the southeastern Atlantic using geostationary satellite observations, Atmos. Chem. Phys., 25, 6957–6973, https://doi.org/10.5194/acp-25-6957-2025, 2025.

Borque, P., Luke, E. P., Kollias, P., and Yang, F.: Relationship between Turbulence and Drizzle in Continental and Marine Low Stratiform Clouds, J. Atmos. Sci., 75, 4139–4148, https://doi.org/10.1175/JAS-D-18-0060.1, 2018.

Cadeddu, M. P., Liljegren, J. C., and Turner, D. D.: The Atmospheric radiation measurement (ARM) program network of microwave radiometers: instrumentation, data, and retrievals, Atmos. Meas. Tech., 6, 2359–2372, https://doi.org/10.5194/amt-6-2359-2013, 2013.

Chen, Y. C., Christensen, M. W., Xue, L., Sorooshian, A., Stephens, G. L., Rasmussen, R. M., and Seinfeld, J. H.: Occurrence of lower cloud albedo in ship tracks, Atmos. Chem. Phys., 12, 8223–8235, https://doi.org/10.5194/acp-12-8223-2012, 2012.

Christensen, M. W. and Stephens, G. L.: Microphysical and macrophysical responses of marine stratocumulus polluted by underlying ships: Evidence of cloud deepening, Journal of Geophysical Research Atmospheres, 116, 1–10, https://doi.org/10.1029/2010JD014638, 2011.

Christensen, M. W., Gettelman, A., Cermak, J., Dagan, G., Diamond, M., Douglas, A., Feingold, G., Glassmeier, F., Goren, T., Grosvenor, D. P., Gryspeerdt, E., Kahn, R., Li, Z., Ma, P.-L., Malavelle, F., McCoy, I. L., McCoy, D. T., McFarquhar, G., Mülmenstädt, J., Pal, S., Possner, A., Povey, A., Quaas, J., Rosenfeld, D., Schmidt, A., Schrödner, R., Sorooshian, A., Stier, P., Toll, V., Watson-Parris, D., Wood, R., Yang, M., and Yuan, T.: Opportunistic experiments to constrain aerosol effective radiative forcing, Atmos. Chem. Phys., 22, 641–674, https://doi.org/10.5194/acp-22-641-2022, 2022.

Clothiaux, E. E., Ackerman, T. P., Mace, G. G., Moran, K. P., Marchand, R. T., Miller, M. A., and Martner, B. E.: Objective Determination of Cloud Heights and Radar Reflectivities Using a Combination of Active Remote Sensors at the ARM CART Sites, Journal of Applied Meteorology, 39, 645–665, https://doi.org/10.1175/1520-0450(2000)039<0645:ODOCHA>2.0.CO;2, 2000.

https://doi.org/10.5194/egusphere-2026-2430
Preprint. Discussion started: 11 June 2026

Cook, D. R. and Sullivan, R. C.: Eddy Correlation Flux Measurement System (ECOR) Instrument Handbook, DOE/SC-ARM-TR-052, 17 pp., 2020.

Diamond, M. S., Director, H. M., Eastman, R., Possner, A., and Wood, R.: Substantial Cloud Brightening From Shipping in Subtropical Low Clouds, AGU Advances, 1, 1–28, https://doi.org/10.1029/2019av000111, 2020.

Fielding, M. D., Chiu, J. C., Hogan, R. J., Feingold, G., Eloranta, E., O'Connor, E. J., and Cadeddu, M. P.: Joint retrievals of cloud and drizzle in marine boundary layer clouds using ground-based radar, lidar and zenith radiances, Atmos. Meas. Tech., 8, 2663–2683, https://doi.org/10.5194/amt-8-2663-2015, 2015.

Gallo, F., Uin, J., Springston, S., Wang, J., Zheng, G., Kuang, C., Wood, R., Azevedo, E. B., McComiskey, A., Mei, F., Theisen, A., Kyrouac, J., and Aiken, A. C.: Identifying a regional aerosol baseline in the eastern North Atlantic using collocated measurements and a mathematical algorithm to mask high-submicron-number-concentration aerosol events, Atmos. Chem. Phys., 20, 7553–7573, https://doi.org/10.5194/acp-20-7553-2020, 2020.

Gelaro, R., McCarty, W., Suárez, M. J., Todling, R., Molod, A., Takacs, L., Randles, C. A., Darmenov, A., Bosilovich, M. G., Reichle, R., Wargan, K., Coy, L., Cullather, R., Draper, C., Akella, S., Buchard, V., Conaty, A., da Silva, A. M., Gu, W., Kim, G.-K., Koster, R., Lucchesi, R., Merkova, D., Nielsen, J. E., Partyka, G., Pawson, S., Putman, W., Rienecker, M., Schubert, S. D., Sienkiewicz, M., and Zhao, B.: The Modern-Era Retrospective Analysis for Research and Applications, Version 2 (MERRA-2), J. Clim., 30, 5419–5454, https://doi.org/10.1175/JCLI-D-16-0758.1, 2017.

George, R. C. and Wood, R.: Subseasonal variability of low cloud radiative properties over the southeast Pacific Ocean, Atmos. Chem. Phys., 10, 4047–4063, https://doi.org/10.5194/acp-10-4047-2010, 2010.

Ghate, V. P., Surleta, T., Magaritz-Ronen, L., Raveh-Rubin, S., Gallo, F., Carlton, A. G., and Azevedo, E. B.: Drivers of Cloud Condensation Nuclei in the Eastern North Atlantic as Observed at the ARM Site, Journal of Geophysical Research: Atmospheres, 128, https://doi.org/10.1029/2023JD038636, 2023.

Goren, T., Choudhury, G., Kretzschmar, J., and McCoy, I.: Co-variability drives the inverted-V sensitivity between liquid water path and droplet concentrations, Atmos. Chem. Phys., 25, 3413–3423, https://doi.org/10.5194/acp-25-3413-2025, 2025.

Gryspeerdt, E., Goren, T., and Smith, T. W. P.: Observing the timescales of aerosol-cloud interactions in snapshot satellite images, Atmos. Chem. Phys., 21, 6093–6109, https://doi.org/10.5194/acp-21-6093-2021, 2021.

Hahn, C. J. and Warren, S. G.: A gridded climatology of clouds over land (1971–96) and ocean (1954–97) from surface observations worldwide, https://doi.org/10.3334/CDIAC/cli.ndp026e, 2007.

Heffter, JL.: Transport Layer Depth Calculations, in: Second Joint Conference on Applications of Air Pollution Meteorology, 1980.

Hersbach, H., Bell, B., Berrisford, P., Hirahara, S., Horányi, A., Muñoz-Sabater, J., Nicolas, J., Peubey, C., Radu, R., Schepers, D., Simmons, A., Soci, C., Abdalla, S., Abellan, X., Balsamo, G., Bechtold, P., Biavati, G., Bidlot, J., Bonavita, M., De Chiara, G., Dahlgren, P., Dee, D., Diamantakis, M., Dragani, R., Flemming, J., Forbes, R., Fuentes, M., Geer, A., Haimberger, L., Healy, S., Hogan, R. J., Hólm, E., Janisková, M., Keeley, S., Laloyaux, P., Lopez, P., Lupu, C., Radnoti, G., de Rosnay, P., Rozum, I., Vamborg, F., Villaume, S., and Thépaut, J.: The ERA5 global reanalysis, Quarterly Journal of the Royal Meteorological Society, 146, 1999–2049, https://doi.org/10.1002/qj.3803, 2020.

Hu, S., Zhu, Y., Rosenfeld, D., Mao, F., Lu, X., Pan, Z., Zang, L., and Gong, W.: The Dependence of Ship-Polluted Marine Cloud Properties and Radiative Forcing on Background Drop Concentrations, Journal of Geophysical Research: Atmospheres, 126, 1–13, https://doi.org/10.1029/2020JD033852, 2021.

Hudson, J. G., Noble, S., and Jha, V.: Stratus cloud supersaturations, Geophys. Res. Lett., 37, 1–4, https://doi.org/10.1029/2010GL045197, 2010.

Kivekäs, N., Massling, A., Grythe, H., Lange, R., Rusnak, V., Carreno, S., Skov, H., Swietlicki, E., Nguyen, Q. T., Glasius, M., and Kristensson, A.: Contribution of ship traffic to aerosol particle concentrations downwind of a major shipping lane, Atmos. Chem. Phys., 14, 8255–8267, https://doi.org/10.5194/acp-14-8255-2014, 2014.

https://doi.org/10.5194/egusphere-2026-2430
Preprint. Discussion started: 11 June 2026

Kyrouac, J. and Tuftedal, M.: Surface Meteorological System (MET) Instrument Handbook, DOE/SC-ARM-TR-086, 2024.

Lewis, E. R.: Marine ARM GPCI investigation of clouds (MAGIC) field campaign report, DOE Office of Science Atmospheric Radiation Measurement (ARM) Program, DOE/SC-ARM-16-057, 2016.

Long, C. N. and Shi, Y.: The QCRad Value Added Product: Surface Radiation Measurement Quality Control Testing, Including Climatology Configurable Limits, the U.S. Department of Energy, DOE/SC-ARM/TR-074, 2006.

Mace, G. G., Benson, S., Gombert, P., and Smallwood, T.: Impact on cloud properties of reduced-sulphur shipping fuel in the Eastern North Atlantic, Atmos. Chem. Phys., 26, 1041–1051, https://doi.org/10.5194/acp-26-1041-2026, 2026.

Minnis, P., Nguyen, L., Palikonda, R., Heck, P. W., Spangenberg, D. A., Doelling, D. R., Ayers, J. K., Smith, Jr., W. L., Khaiyer, M. M., Trepte, Q. Z., Avey, L. A., Chang, F.-L., Yost, C. R., Chee, T. L., and Szedung, S.-M.: Near-real time cloud retrievals from operational and research meteorological satellites, https://doi.org/10.1117/12.800344, 7107, 19–26, https://doi.org/10.1117/12.800344, 2008.

Morris, V. R.: Ceilometer Instrument Handbook, U.S. Department of Energy, Atmospheric Radiation Measurement user facility, DOE/SC-ARM-TR-149, 2016.

Mülmenstädt, J., Ackerman, A. S., Fridlind, A. M., Huang, M., Ma, P., Mahfouz, N., Bauer, S. E., Burrows, S. M., Christensen, M. W., Dipu, S., Gettelman, A., Leung, L. R., Tornow, F., Quaas, J., Varble, A. C., Wang, H., Zhang, K., and Zheng, Y.: Can general circulation models (GCMs) represent cloud liquid water path adjustments to aerosol–cloud interactions?, Atmos. Chem. Phys., 24, 13633–13652, https://doi.org/10.5194/acp-24-13633-2024, 2024.

Newsom, R., Sivaraman, C., Shippert, T., and Riihimaki, L.: Doppler Lidar Vertical Velocity Statistics Value-Added Product, Richland, Washington, 2025.

Norris, J. R. and Iacobellis, S. F.: North pacific cloud feedbacks Inferred from synoptic-scale dynamic and thermodynamic relationships, J. Clim., 18, 4862–4878, https://doi.org/10.1175/JCLI3558.1, 2005.

Qiu, S., Zheng, X., Painemal, D., Terai, C. R., and Zhou, X.: Daytime variation in the aerosol indirect effect for warm marine boundary layer clouds in the eastern North Atlantic, Atmos. Chem. Phys., 24, 2913–2935, https://doi.org/10.5194/acp-24-2913-2024, 2024.

Randall, D. A., Coakley, J. A., Lenschow, D. H., Fairall, C. W., and Kropfli, R. A.: Outlook for research on subtropical marine stratification clouds, Bull. Am. Meteorol. Soc., 65, 1290–1301, https://doi.org/10.1175/1520-0477(1984)065<1290:OFROSM>2.0.CO;2, 1984.

Rolph, G., Stein, A., and Stunder, B.: Real-time Environmental Applications and Display sYstem: READY, Environmental Modelling & Software, 95, 210–228, https://doi.org/10.1016/j.envsoft.2017.06.025, 2017.

Russell, L., Lubin, D., Silber, I., Eloranta, E., Muelmenstaedt, J., Burrows, S., Aiken, A., Wang, D., Petters, M., Miller, M., Ackerman, A., Fridlind, A., Witte, M., Lebsock, M., Painemal, D., Chang, R., Liggio, J., and Wheeler, M.: Eastern Pacific Cloud Aerosol Precipitation Experiment (EPCAPE) Science Plan, Doe/Sc-Arm-21-009, 2021.

Stein, A. F., Draxler, R. R., Rolph, G. D., Stunder, B. J. B., Cohen, M. D., and Ngan, F.: NOAA's HYSPLIT Atmospheric Transport and Dispersion Modeling System, Bull. Am. Meteorol. Soc., 96, 2059–2077, https://doi.org/10.1175/BAMS-D-14-00110.1, 2015.

Toll, V., Christensen, M., Quaas, J., and Bellouin, N.: Weak average liquid-cloud-water response to anthropogenic aerosols, Nature, 572, 51–55, https://doi.org/10.1038/s41586-019-1423-9, 2019.

Turner, D. D., Clough, S. A., Liljegren, J. C., Clothiaux, E. E., Cady-Pereira, K. E., and Gaustad, K. L.: Retrieving liquid water path and precipitable water vapor from the atmospheric radiation measurement (ARM) microwave radiometers, in: IEEE Transactions on Geoscience and Remote Sensing, 3680–3689, https://doi.org/10.1109/TGRS.2007.903703, 2007.

Twomey, S.: The Influence of Pollution on the Shortwave Albedo of Clouds, J. Atmos. Sci., 34, 1149–1152, https://doi.org/10.1175/1520-0469(1977)034<1149:TIOPOT>2.0.CO;2, 1977.

https://doi.org/10.5194/egusphere-2026-2430
Preprint. Discussion started: 11 June 2026

Uin, J. and Enekwizu, O.: Cloud Condensation Nuclei Particle Counter Instrument Handbook, DOE/SC-ARM-TR-168, 2024.

Wang, H., Rasch, P. J., and Feingold, G.: Manipulating marine stratocumulus cloud amount and albedo: A process-modelling study of aerosol-cloud-precipitation interactions in response to injection of cloud condensation nuclei, Atmos. Chem. Phys., 11, 4237–4249, https://doi.org/10.5194/acp-11-4237-2011, 2011.

Wang, J., Wood, R., Jensen, M., Azevedo, E., Bretherton, C., Chand, D., Chiu, C., Dong, X., Fast, J., and Gettelman, A.: Aerosol and cloud experiments in eastern North Atlantic (ACE-ENA) field campaign report, DOE Office of Science Atmospheric Radiation Measurement (ARM) Program, DOE/SC-ARM-19-012, 2019.

Warren, S. G., Hahn, C. J., London, J., Chervin, R. M., and Jenne, R. L.: Global distribution of total cloud cover and cloud type amounts over the ocean, 1988.

Widener, K., Bharadwaj, N., and Johnson, K.: Ka-Band ARM Zenith Radar (KAZR) Instrument Handbook, https://doi.org/10.2172/1035855, 2012.

Xie, S., McCoy, R. B., Klein, S. A., Cederwall, R. T., Wiscombe, W. J., Jensen, M. P., Johnson, K. L., Clothiaux, E. E., Gaustad, K. L., Long, C. N., Mather, J. H., McFarlane, S. A., Shi, Y., Golaz, J.-C., Lin, Y., Hall, S. D., McCord, R. A., Palanisamy, G., and Turner, D. D.: CLOUDS AND MORE: ARM Climate Modeling Best Estimate Data, Bull. Am. Meteorol. Soc., 91, 13–20, https://doi.org/10.1175/2009BAMS2891.1, 2010.

Yuan, T., Song, H., Wood, R., Oreopoulos, L., Platnick, S., Wang, C., Yu, H., Meyer, K., and Wilcox, E.: Observational evidence of strong forcing from aerosol effect on low cloud coverage, Sci. Adv., 9, 1–10, https://doi.org/10.1126/SCIADV.ADH7716, 2023.

Yuan, T., Song, H., Oreopoulos, L., Wood, R., Bian, H., Breen, K., Chin, M., Yu, H., Barahona, D., Meyer, K., and Platnick, S.: Abrupt reduction in shipping emission as an inadvertent geoengineering termination shock produces substantial radiative warming, Commun. Earth Environ., 5, 1–8, https://doi.org/10.1038/s43247-024-01442-3, 2024.

Yuan, T., Song, H., Oreopoulos, L., Wood, R., Meyer, K., Crawford, A., Smith, W., and Eastman, R.: Analyses of Virtual Ship-Tracks Systematically Underestimate Aerosol-Cloud Interactions Signals, Geophys. Res. Lett., 52, https://doi.org/10.1029/2024GL114356, 2025a.

Yuan, T., Song, H., Boss, L. F., and Diamond, M. S.: Detectable ship tracks account for just 5% of aerosol indirect forcing from ship emissions, Commun. Earth Environ., 6, https://doi.org/10.1038/s43247-025-02825-w, 2025b.